Morphology and Pathology of the Cysteine Dioxygenase Knockout Mouse:
Evaluating Skeletal and Connective Tissue Abnormalities

Honors Thesis
Presented to the College of Agriculture and Life Sciences
Division of Nutritional Sciences
of Cornell University
in Partial Fulfillment of the Requirements for the
Research Honors Program

by
Jimmy Lam
May 2011

Martha H. Stipanuk, Ph.D.

Acknowledgements

Foremost, I would like to thank my research advisor, Dr. Martha H. Stipanuk, for her generous support throughout my undergraduate studies. Without her kindness and provision, none of my undergraduate endeavors would have been possible. Dr. Stipanuk served as a mentor, academic advisor, research advisor, and as a professor. I will never forget her willingness to reach out to students, staff, and acquaintances on a personal level. She is a rare welcoming muse on Cornell's campus.

Secondly, it is with great honor and pleasure to have met and worked under the tutelage of Heather B. Roman and Lawrence L. Hirschberger, both who have contributed significantly to the expansion of my practical skills in the laboratory environment. Heather was the primary contributor to my thesis direction and contributed significantly to the histology and PCR work presented in this thesis. She also bestowed upon me much background knowledge in anatomy that I otherwise would not have received in my general education. Larry had the answers to all of my inquiries and was willing to put aside his experiments to answer my questions. He was the first to demonstrate how the lab functions. Honing my technical skills would not have been possible without his vigilance. His patience is the catalyst for my continued interests in laboratory sciences. Larry is also the backbone to the Stipanuk Laboratory.

As for my extended interests aside from human medicine in the humanities, life sciences, human rights, global/public health, writing, and culture, I could not thank enough those who have inspired me. Cornell University, Dr. Dotsevi Sogah, Gabriela Wagner, Jamie Moore, Dr. Shu-Bing Qian, Alice Lu, Carolyn Junior, Eric Przybyzewski, Stella Lam, Mommy and Daddy, Dr. Laura Harrington, Tim Burton, Dr. Marie Caudill, and Professor Cynthia Blake Thompson will always remain permanent reminders of why I am pursuing a career as a physician.

Generous funding was provided by the Morley Student Research Fund and the Dextra Undergraduate Research Endowment Fund.

The Lab of Ornithology and the Qi Laboratory graciously welcomed collaborations, allowing my use of x-ray and DEXA equipment, respectively.

ABSTRACT

Cysteine catabolism is dependent upon cysteine dioxygenase (CDO), a thiol dioxygenase encoded by the gene *CDO1*. The clinical literature and, more recently, the study of CDO polymorphisms in disease and control populations have illustrated a strong association of impaired metabolism of cysteine to sulfate and taurine and/or CDO loss-of-function mutations with a variety of autoimmune and neurodegenerative diseases. The Stipanuk research group has recently generated a germ-line CDO knockout ($CDO^{-/-}$) mouse that clearly has metabolic and phenotypic abnormalities. Phenotypically, CDO knockout (null) mice exhibit signs of connective tissue and skeletal abnormalities, especially joint hyperlaxity (hypermobility) and wry nose (contortions in the nasal bone). Our studies indicate that CDO null mice have clear connective tissue abnormalities. Key abnormal features include significant increases in lung air space, measured by mean linear intercept; lung elastic fiber disarray and entanglement; significant increase in matrix metalloproteinase-12 (MMP-12), an enzyme involved in degrading elastin, in the lung; and skeletal development retardation.

LITERATURE REVIEW

Cysteine Metabolism

Cysteine is a sulfur amino acid utilized both for the synthesis of proteins and the synthesis of essential non-protein compounds, which include glutathione, taurine, pyruvate and sulfate. Key enzymes involved in the catabolism of cysteine to the non-protein compounds include glutamate-cysteine ligase, cystathionine □-lyase, cystathionine □-synthase, cysteinesulfinate decarboxylase, and cysteine dioxygenase (CDO) (1). The activity of most of these enzymes is highest in liver, the organ that plays a central role in metabolizing cysteine (2). The CDO pathway is the first step in the oxidative catabolism of cysteine, yielding cysteinesulfinate, which can be further catabolized to sulfate and pyruvate or to taurine. In response to high levels of dietary protein or sulfur amino acids, hepatic CDO of mice undergoes up to a 30-fold change in concentration and up to 10-fold changes in catalytic efficiency, translating to an overall 300-fold increase in catalytic CDO activity (1,3,4,5). This abundant regulation of CDO suggests that control of cysteine concentration is crucial to living organisms.

CDO not only removes excess cysteine but is necessary to meet the physiological demands for inorganic sulfate and taurine. High plasma cysteine levels and low plasma sulfate levels have been associated with severity and rapid progression of rheumatoid arthritis and with incidence of several neurological diseases (6). The study of CDO polymorphisms in disease and control populations has provided further support for a strong association of CDO genetic polymorphisms with rheumatoid arthritis (7). The Stipanuk group has generated germ-line CDO knockout or null mice ($CDO^{-/-}$) that clearly have metabolic and phenotypic abnormalities. Phenotypically, CDO null mice exhibit signs of connective tissue and skeletal abnormalities.

Bone Development

Connective tissue, a constituent within the extracellular matrix (ECM), confers the form and strength to tissues. Connective tissue is commonly made up of collagen, hyaline, elastin fibers, fibronectins, laminins, and proteoglycans. Connective tissue may be loose (e.g. the tissue that holds organs in place and attaches epithelial tissue to other underlying tissues), fibrous, cartilaginous, or dense (e.g. tendons, ligaments, and compact/cancellous bone).

Skeletal development in vertebrates, which includes both ossified bone and cartilage, has its roots from three distinct embryonic lineages (8). Relevant to our study is the development of the craniofacial, axial, and limb skeleton. The craniofacial skeleton has its origins from the cranial neural crest; the axial skeleton has its origins from the somites; and the limb skeleton has its origins from the lateral plate mesoderm (Figure 1).

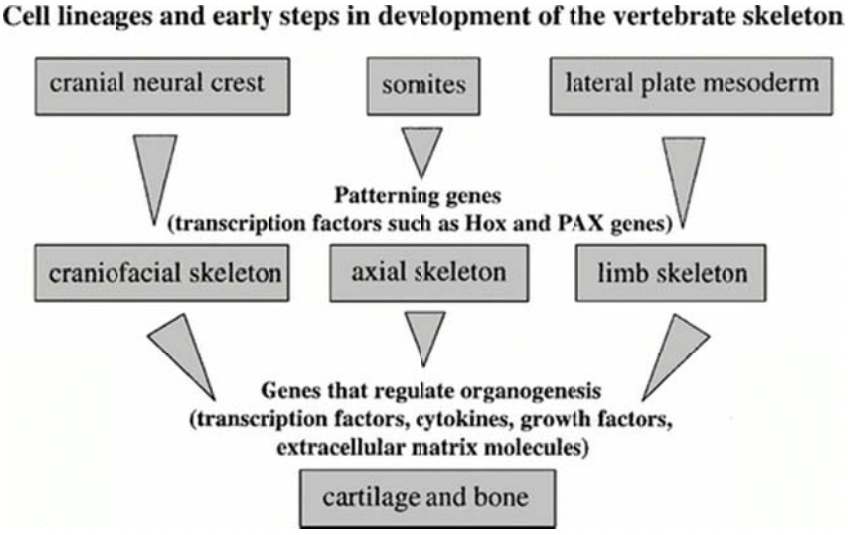

Figure 1. Diagram illustrates the nature of organogenesis from pre-cursor cells. Figure also demonstrates the factors involved in promoting organogenesis. Diagram from Olsen et al. (8).

In our study, particular interest was focused on the craniofacial abnormalities in CDO null mice. During the craniofacial skeletal development, cells from the dorsal region of the

neural tube migrate from the branchial arches and frontonasal mass (9). These cells then make up the cartilage and bone of the craniofacial skeleton. Examples of craniofacial structures that the neural crest cells generate include the frontal and parietal bones. The process of neural crest cell differentiation into craniofacial skeletal structures depends on cytokine signaling to the epithelial cells. The mesenchyme cells, which are pluripotent stem cells, receive downstream cytokine signals from the epithelial cells before secreting their own signals to promote the growth and differentiation of neural crest cells into craniofacial structures (9).

Ossification in the mouse skeleton occurs between days 14 and 15 after fertilization (10,11). For this particular study, interest was in the skeletal features of the cranium, sternebrae, and femur of CDO null and wild-type ($CDO^{+/+}$) mice. Renditions of these skeletal features are displayed in Figure 2. The skull and extremities of the mouse fetus are normally fully ossified two days before birth (12). Mice have six sternebrae numbered 1-6. By convention, the sternebrae are labeled from the most cephalic sternebra (sternebra 1) to the most caudal sternebra (sternebra 6). Most of the sternebrae are fully ossified in each of their unilateral ossification center at birth, but sternebra 5 tends to lag behind in becoming fully ossified. A study found that in a cohort of 67 mice, all mice had fully unilaterally ossified sternebra 5 by post natal day (PND) 12 (12). Since the mice used in our study were between PND 54 and PND 61, we assumed that all unilateral ossification centers were fully ossified. Our focus was not on the unilateral fusion of a single sternebra. Instead, our focus was on observing the fusion that joins two sternebrae (sternebra 4 and sternebra 5) at the juncture that they meet.

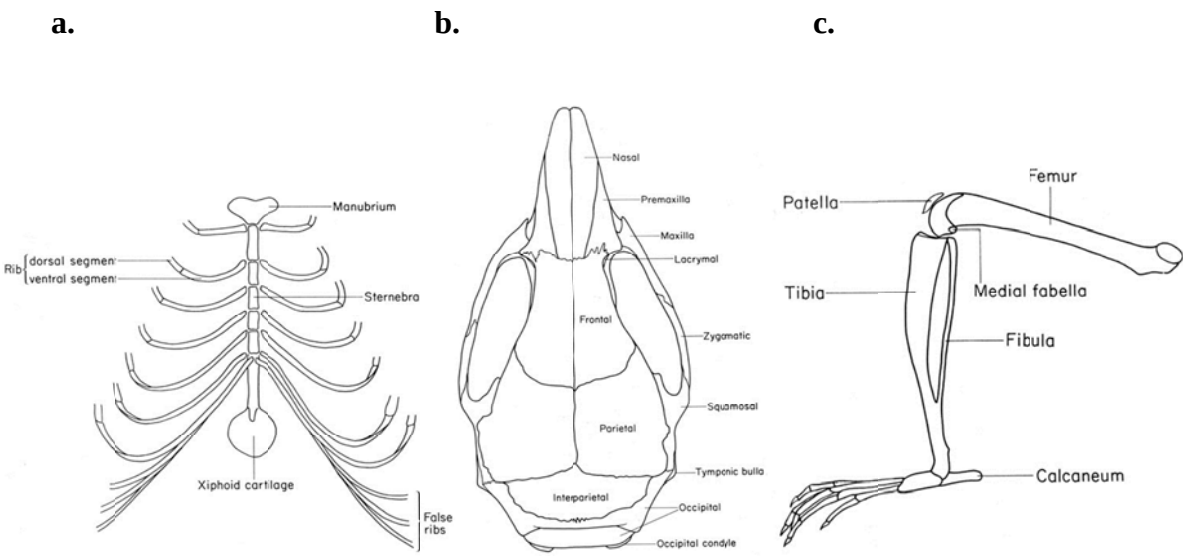

Figure 2. Select skeletal structures of mice. (a) Ventral aspect of sternum and rib; (b) Dorsal aspect of skull; (c) Medial aspect of right hind limb. Images adopted from www.informatics.jax.org.

Lung

The lower respiratory tract contains the lungs, an organ rich in connective tissue required for respiration. The passageway of airflow is directed in the following pathway, going from the largest to the smallest structures: orifices (i.e. nose and mouth), trachea, bronchi, bronchioles, respiratory bronchioles, alveolar duct, alveolar sac and individual alveolus. Air flow structures with cartilage are known as bronchi. With no cartilage, it is called a bronchiole. The alveolar duct contains a collection of alveoli. The alveolus is a space occupied by air. Gas exchange between blood and air occurs at the beginning of the respiratory bronchiole and ending at the alveoli. Gas exchange occurs through small apertures 7-8μm in diameter in the interalveolar walls that separate alveoli. Capillary beds located behind the basement membrane of the interalveolar walls allow for this gas exchange. The integrity of these interalveolar walls is reinforced by connective tissues including elastic fibers, reticular fibers, and by basement membrane. Flat squamous epithelial cells make up the majority of the interalveolar wall. Space

between the basement membrane of epithelial cells and that of capillaries allows cells like macrophages to enter (13). See Figure 3a for a histological interpretation of a normal lung.

The capillary beds receive their oxygenated blood from the air inspired. Oxygenated blood is sent out of the lungs by the pulmonary vein. Deoxygenated blood is collected and removed by the pulmonary artery. From the lumen of the artery to the basal portion of the blood vessel, distinct layers are labeled as tunica intima, tunica media, and tunica externa (Figure 3b). This nomenclature also applies to the vein. The connective tissue features of the lung mark the lungs as an ideal specimen for connective tissue studies. The tunica intima is composed of endothelium, collagen, and elastic fibers. An elastic lamina separates the tunic intima from the tunica media. The tunica media houses the smooth muscles within a matrix of thin elastic fibers. The tunica media is thinner in veins than in arteries. The tunica adventitia is composed of connective tissue and small nerves. The tunica adventitia in veins is much wider than in arteries (14). See Figure 3b for histology of the artery and vein.

a. **b.**

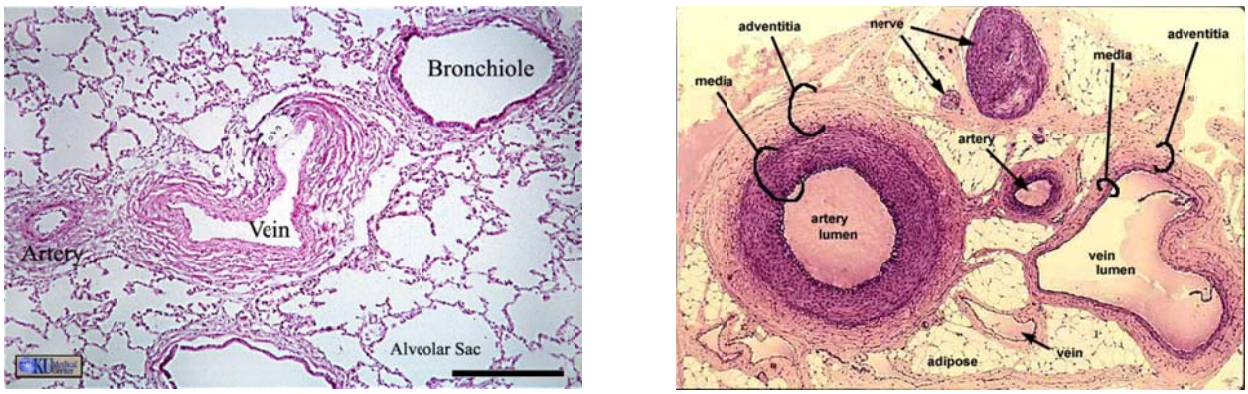

Figure 3. (a) Normal histology of lung. Image adopted from http://www.kumc.edu/instruction/medicine/anatomy/histoweb/resp/resp.htm (scale bar is 250μm); (b) Normal histology of artery and vein. Image adopted from http://legacy.owensboro.kctcs.edu/gcaplan/anat2/histology/histo%20G%20cardiovascular.htm.

Connective Tissue Remodeling

Matrix Metalloproteinases

Embryonic development and postnatal maturation depend on continual turnover of connective tissue. Connective tissue turnover involves proteolytic processes accomplished by matrix metalloproteinases (MMPs) and regulated by their inhibitors, otherwise known as the tissue inhibitors of metalloproteinases (TIMPs) (15,16,17). MMPs are a family of highly homologous zinc endopeptidases that not only degrade protein components of the ECM but also have dynamic roles in normal physiological functions (like the menstrual cycle). There functions also extend towards diseases involving abnormal ECM turnover like arthritis, cancer, and sepsis (18,19,20,21,22). MMPs may also function to process bioactive molecules such as cytokines, apoptotic ligands, and cell surface receptors (23,24,25).

To date, at least 25 MMPs have been identified. Cumulatively, the MMPs cleave all of the proteins found in the ECM, including mineralized matrices (26,27). All MMPs identified thus far can be categorized by eight distinct structural groups (28). These eight distinct MMPs may further be categorized as membrane-bound or secreted. Common to each of the matrix metalloproteinases, however, are three domains: signal peptide, propeptide, and the catalytic domain (Figure 4).

Figure 4. Figure depicts the core domains of all matrix metalloproteinases. Figure from Sternlicht and Werb (28).

The catalytic region of the MMPs also houses the zinc-binding region. All MMPs contain a highly conserved region in the catalytic domain that constitutes a calcium-binding site.

The addition of extra domains to the core domains of the MMPs characterizes the idiosyncrasies of each type of MMP.

In addition to structural similarities, MMPs are often classified based on functional similarities as follows: collagenases (MMP-1,-8,-13); gelatinase (MMP-2,-9); stromelysins (MMP-3,-10,-11); matrilysins (MMP-7,-26); membrane-type (MT-MMP-14,-15,-16,-17,-24,-5); and others (MMP-12 is considered a macrophage elastase) (29).

Two MMPs relevant to this study are MMP-9 and MMP-12. Most MMPs do not have any one particular substrate. Subsequently, a MMP like gelatinase (MMP-9) cleaves a variety of proteinaceous ECM components, including plasminogen, gelatin, elastin, and collagen (Type IV, V, XI and XIV) (30). As another example, MMP-12 cleaves collagen (IV and V), gelatin, elastin, and fibronectin (31). MMP-9 is produced primarily by epithelial cells and macrophages (32). MMP-12 is primarily produced by macrophages and targets the epithelial cells (33,34). Our attention to MMP-9 and MMP-12 was localized to the lungs of CDO null mice, where connective tissue pathology was apparent. Imbalances in the MMPs have been recorded to result in lung pathology, including chronic inflammation, emphysema, and chronic obstructive pulmonary disease. Specifically, lungs with an up-regulation of MMP-9 and MMP-12 have been accompanied by the disarray seen in emphysemic and fibrotic lungs (35,36). Our selective attention to MMP-9 and MMP-12 is fitting to their role in degrading collagen and elastin, a normal physiological process that presented itself pathologically in histological images of our CDO null mice. Equally as important as the MMPs are the TIMPs, which act antithetical to MMPs by inhibiting the MMPs. Dysregulation seen from ECM pathology is not solely

dependent on the up-regulation or the down-regulation of any one MMP or any one TIMP but by the nexus and homeostatic balances between the MMPs and TIMPs.

Tissue Inhibitors of Matrix Metalloproteinases

Tissue inhibitors of matrix metalloproteinases (TIMPs) are specific inhibitors of MMPs that control the proteolytic activity of MMPs in tissues. TIMPs bind MMPs in a 1:1 ratio and are equally as important as MMPs are for development and tissue remodeling. The stoichiometric ratio prevents MMPs from catalyzing excessive degradation of connective tissue proteins, while allowing connective tissue formation to occur. At the time of this study, four TIMPs have been classified in vertebrates (TIMP-1, TIMP-2, TIMP-3, and TIMP-4) (37,38). Like MMPs, TIMPs have other biological functions in addition to the MMP inhibitory function they were named after. For instance, TIMP-1 and TIMP-2 have erythroid-potentiating and cell growth activity (39,40); TIMP-3 regulates inflammation (41); and TIMP-4 has been found to be cardio-protective (42). In our attempts to evaluate homeostatic imbalances in MMP-9 and MMP-12, we used TIMP-1 and TIMP-3 for their known function to inhibit both of the MMPs under study. Moreover, TIMP-1 inhibits the activity of most MMPs with the exception of MT1-MMP and MMP-2 (43). Thus, any dysregulation of TIMP-1 may have a broader implication than simply an effect on MMP-12. TIMP-3 inhibits MMPs-1,-2,-3,-9, and -13 and was selected based on its anti-inflammatory functions (41,44). Thus, if damage in the lung of our mice is due to inflammation, dysregulation of TIMP-3 may be a suspect.

METHODS

Generation of mice

Mice were housed in a pathogen free barrier facility. All animals had access to an irradiated standard non-purified rodent diet (7012 Teklad LM-485, Harlan Laboratories, Inc.) (except when a non-purified diet is indicated) and water *ad libitum*. Male and female mice heterozygous for the null CDO allele were intercrossed to generate wild-type ($CDO^{+/+}$), heterozygous ($CDO^{+/-}$) and null ($CDO^{-/-}$) mice. Animals were genotyped at postnatal day 14 (PND 14) and weaned at PND 28, as described previously (64). All experimental procedures involving mice were approved by the Cornell University Institutional Animal Care and Use Committee.

Morphometric analysis of skeletal structure

Wild-type (WT) and null mice (n=53: 14 null females, 12 WT females, 16 null males, 11 WT males) were euthanized by carbon dioxide inhalation when they were approximately eight weeks of age (ranging from 51 to 64 days of age). Whole skeletons were prepared by the method of Depew (45). Whole mice were dehydrated by incubating in 95% ethanol for two hours. They were then removed from the ethanol, skinned, and eviscerated. Muscle and connective tissues were left intact. Specimens were then further incubated in 95% ethanol for five days, followed by incubation in acetone for six days for further dehydration and removal of fat. The following cranial measurements, as suggested by Kawakami (46), were then made on the cranium of mice specimens using an electronic digital caliper (Fisher Scientific, PA): nasal bone length, frontal bone length, parietal bone length, interparietal bone length, nasal bone

width, distance between left and right anterolateral corner of the frontal bone, frontal bone width, and interparietal bone width.

Skeletal staining procedure

After documenting cranial measurements, specimens were immediately placed in a staining solution containing Alizarin Red (0.005%, w/v) and Alcian Blue (0.015%, w/v) dye for five days (46). The mice were then transferred to a 1% (w/v) KOH solution. The KOH solution was renewed three times over the course of six days in order to remove excess staining, soften the skeletal structure, and remove non-skeletal structures like muscles and adipose tissue. This was followed by the sequential replacement of KOH with glycerol over the course of two weeks. Glycerol-1% (w/v) KOH solutions with decreasing ratios of glycerol-to-KOH replaced older solutions: the ratio of glycerol-to-1% KOH that was added over the course of two weeks was as follows: 1:4, 1:1, 4:1, and finally 100% glycerol. This procedure resulted in clearly visible stained bone and cartilage. Specimens were then stored in 50-mL conical tubes containing glycerol until observations were made.

Histomorphometric evaluation of differentially stained lung sections

CDO null and wild-type animals were anesthetized by intraperitoneal injection of Avertin® (tribromomethanol). Next, a scalpel blade was used to open the abdominal cavity and cut the diaphragm, and lungs were perfused intratracheally with a blunt butterfly catheter connected to a column of 4% (v/v) paraformaldehyde suspended 25 cm above the dissecting surface. When the lungs were fully inflated with paraformaldehyde, the trachea was clamped, and the entire mass of thoracic viscera was removed intact and placed in 4% paraformaldehyde for 24 hours. Samples from two or more lung lobes of each mouse were submitted for

histological processing (Electron Microscopy and Histology Core Facility, Cornell University). Semi-serial, 5-μM sections from paraffin embedded tissues were processed with Verhoeff VanGeison (VVG), Hematoxylin and Eosin (H&E) stains to visualize and compare connective tissue components. Stained sections were analyzed using an Olympus BX50 microscope with a Moticam 2300 cMOS camera (Motic North America, Richmond, BC). Images from the Moticam 2300 cMOS camera were analyzed at 200x magnification using JMicroVision 1.2.7 (http://www.jmicrovision.com) to evaluate mean linear intercept (MLI), a measure of the distance between interalveolar walls, by the method of Dunnill (47) with modifications by Hamelet et al. (48). A large MLI indicates airspace enlargement in the alveoli and consequently reduced surface area for gas exchange. In brief, the mean linear intercept value was calculated by obtaining an average of 5-9 images from lung specimens prepared for each mouse at 200x magnification. Images were overlaid with a scaled 50-μM grid (approximately 10 vertical lines x 10 horizontal lines). A sum of the number of alveolar walls intersected by lines in both the horizontal and vertical direction was divided by the total length of the lines on each image, yielding the MLI value. A representative MLI for each animal was determined by averaging the MLI values over all images counted for that animal.

Analysis of MMP-9, MMP-12, TIMP-1, and TIMP-3 expression by Western blotting and real time quantitative RT-PCR (qRT-PCR)

For collection of tissues for analysis of expression of matrix metalloproteinases (MMPs) and tissue inhibitors of metalloproteinases (TIMPs), null and wild-type mice were both placed on a semi-purified rodent diet at weaning and then switched to a diet with a slightly excess level of sulfur amino acids at 6-7 weeks of age. These semi-purified diets were based on the AIN93G formulation with the control diet containing 200 g isolated soy protein + 3.1 g L-methionine per

kg (8.0 methionine equivalents per kg) and the sulfur amino acid-enriched diet containing 200 g vitamin-free casein + 4.2 g L-cystine + 1.5 g L-methionine (12.3 methionine equivalents per kg). [For reference, the standard AIN93G diet formulation for rodents provides 9.3 methionine equivalents per kg, with 1 g cystine = 1.24 g methionine equivalents.] The purpose of the diet enriched in sulfur amino acid content was to enhance the phenotype by giving the mice a higher load of cysteine, the substrate for cysteine dioxygenase. At 8-9 weeks of age (after 2 weeks on the sulfur amino acid-rich diet), mice were euthanized with CO_2 and lungs were collected, immediately frozen in liquid nitrogen, and stored at -80^{o}C.

Samples of frozen tissues were homogenized and Western blotting was performed to determine the protein expression levels of MMP-9, MMP-12, TIMP-1, and TIMP-3 in lungs of null and wild-type mice. For each tissue sample, a homogenate was prepared in lysis buffer [50 mM Tris, pH 7.5, 1% (v/v) Non-idet P-40, 2 mM EDTA, 150 mM NaCl supplemented with 1x mammalian protease inhibitor cocktail (Sigma-Aldrich, MO)]. Homogenates were centrifuged at ~14,000 x *g* at 4°C for 20 min to obtain the supernatant fraction. Protein content of the supernatant was determined using the BCA Protein Assay Kit (Pierce Thermo Scientific, IL) before separating the protein on sodium dodecylsulfate–polyacrylamide gel electrophoresis using a 12% (w/v) polyacrylamide separating gel and 4% stacking gel. The proteins in the separating gel were then transferred onto Immobolin-P polyvinylidene difluoride membrane (Millipor, MA) overnight for 17 hours at 30 V in transfer buffer (25 mM Tris base, 193mM glycine, and 15% (v/v) methanol). After the protein transfer, the Immobolin-P membrane was blocked with blocking buffer (LI-COR, MD) for one hour before incubating overnight with the antibodies of interest. The antibodies used include the following: goat anti-mouse MMP-9 antibody (R&D,

MN), rabbit anti-mouse MMP-12 antibody (Origene, MD), rabbit anti-mouse TIMP-1 antibody (Origene, MD), rabbit anti-mouse TIMP-3 antibody (Abcam, Cambridge, MA), and mouse anti-mouse Actin antibody (Cell Signaling Technology, MA). After incubating with primary antibodies, the membranes were incubated with secondary complementary antibody for one hour. The secondary antibodies were infrared fluorescent dye-labeled anti-mouse, anti-goat, or anti-rabbit IgG antibodies (IRDye, LI-COR Biosciences). Scanning of membranes was in accordance with the manufacturer and the Odyssey direct infrared imaging system (LI-COR Bioscience). The intensity of signals was quantified with Odyssey software (LI-COR Biosciences). Results for MMPs and TIMPs were normalized for actin levels.

Real time quantitative RT-PCR (qRT-PCR) measurements were performed to quantify MMP-9, MMP-12, TIMP-1, and TIMP-3 mRNA levels in the lung tissue samples (n=6: 3 null males, 3 WT males). RNA was isolated using Qiazol and RNeasy Mini Kit with on-column DNAse digest (Qiagen, CA). Concentration of isolated RNA was determined using a NanoDrop spectrophotometer (Thermo Scientific, DE), and 1 μg RNA was reverse transcribed into cDNA using the High-Capacity cDNA Reverse Transcription Kit (Applied Biosystems, CA) according to manufacturer directions. qRT-PCR was performed with a 480 LightCycler PCR System (Roche Applied Science, IN) using Sybr Green Master Mix (Applied Biosystems, CA). Actin was used as the endogenous (housekeeping) control.

Primers were generated by Integrated DNA Technologies (IDT, IA) for target gene MMP-9 (forward primer, AGACGACATAGACGGCATCC; reverse primer, GGCTGTGGTTCTGTTGTGG), target gene MMP-12 (forward primer,

TTGTGGATAAACACTACTGGAGGT; reverse primer, AAATCAGCTTGGGGTAAGCA), target gene TIMP-1 (forward primer, GCAAAGAGCTTTCTCAAAGACC; reverse primer, AGGGATAGATAAAGAGGGAAACAC), and target gene TIMP-3 (forward primer, TGTCGTGCTCCTGAGCTG; reverse primer, GCTTCTTTCCCACCACTTTG.

The average crosspoint (Ct) for each transcript of the target gene and for the standard actin gene were calculated via the LightCycler software (Roche Applied Science, IN). Average actin Ct values were subtracted from the average target values for each animal, yielding ΔCt. Next, ΔΔCt was calculated by subtracting the average WT ΔCt from each animal's ΔCt value. Fold-change was then calculated ($2^{-\Delta\Delta Ct}$). Average values for fold-change were than calculated. Calculations suggested by Pfaffl (49).

Statistical Analysis

Graph Pad Prism 4 Software – Data were analyzed with unpaired one-tail t-test values for cranial measurements, MLI measurements, and quantitative Western blotting measurements between CDO null and wild-type mice. The significance of effects of genotype and sex (and there interaction) on the incidence of abnormal bone features in the sternebrae, nasal bone, and xiphoid cartilage was assessed by a logistic regression (*JMP Statistical Software*). Fisher's exact two-tail test was also used to analyze significance of male and female effects on abnormal phenotype. Results are expressed for main effects as P= # for significance or P=NS for non-significance.

RESULTS

Four cranial landmark measurements highlight bone growth stunting

Lengths of the following cranial landmarks were quantified for all specimens (n=53; 14 CDO null females, 12 wild-type females, 16 CDO null males, 11 wild-type males): nasal bone length (NL), frontal bone length (FL), parietal bone length (PL), interparietal bone length (IL), nasal bone width (NW), left and right corner of frontal bone (LR), frontal bone width (FW), and interparietal bone width (IW). Figure 5 illustrates the various bone lengths and widths measured. A statistically significant difference in four landmarks of cranium size was seen in CDO null mice compared with wild-type mice. The four landmarks were the NL (females, p=0.032; males, p=NS), FL (female, p=0.035; male, p=0.016), NW (female, p=0.030; male, p=0.002), and LR (female, p=NS; male, p=0.002) (Figure 6). In null mice of both sexes, FL was significantly less and NW was significantly greater. On the other hand, NL was significantly less only in CDO null female mice, and LR was significantly less only in CDO null male mice compared to wild-type mice of the same sex.

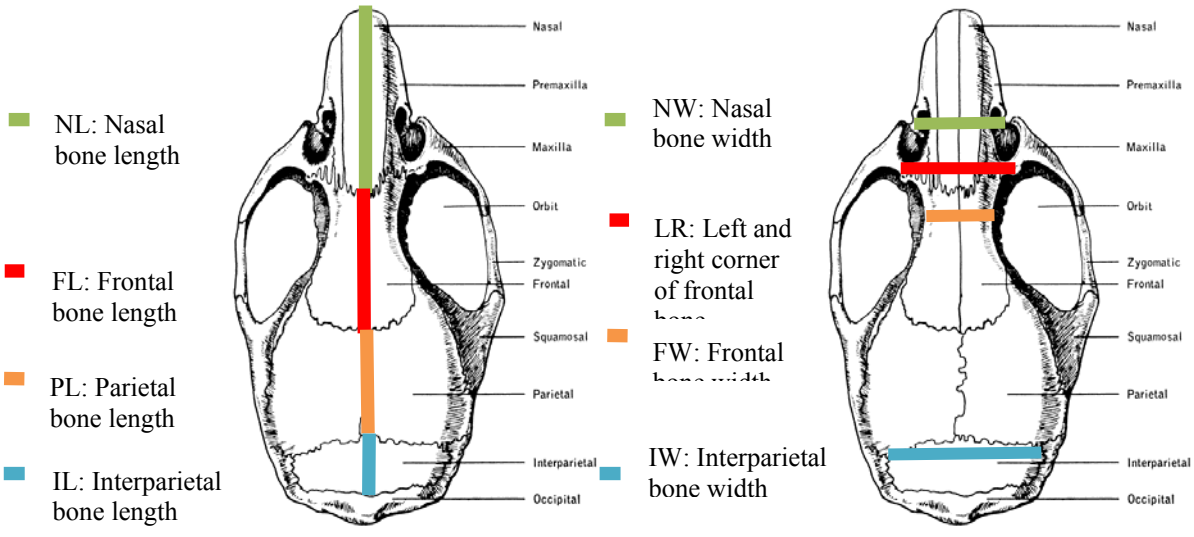

Figure 5. Nomenclature of cranial landmarks from Kawakami and Yamamura (6).

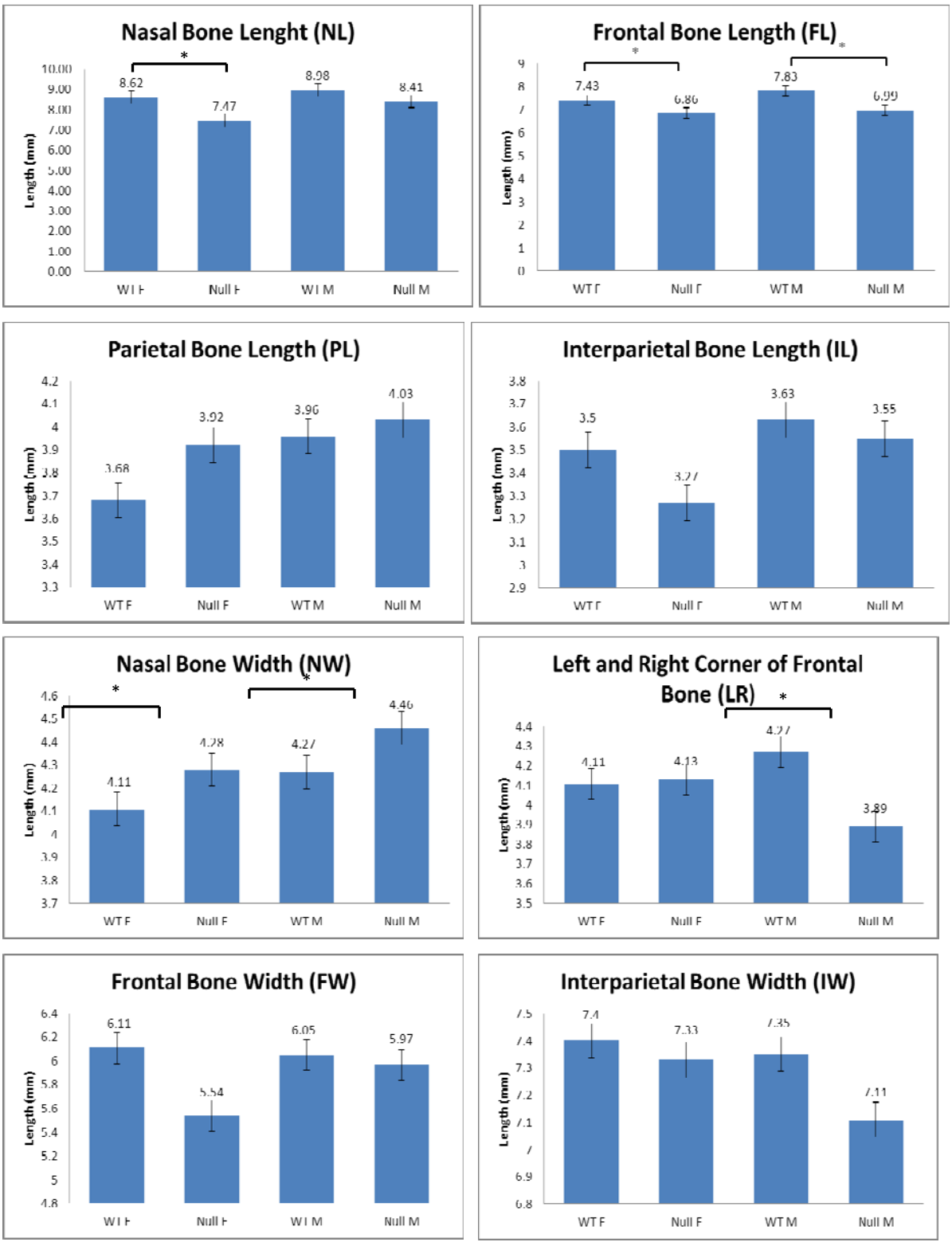

Figure 6. Graphical representation of landmark measurements of the cranium. Measurements with statistical significance were noted. Asterisks indicate $p < 0.050$. Mean data are indicated above each bar ± standard error of mean (SEM). N=53: 14 CDO null females, 12 WT females, 16 CDO null males, 11 WT males.

Skeletal staining identified abnormal formation of bone and poor ossification

Three notable skeletal abnormalities were noted in CDO null mice compared to wild-type mice. These differences are embodied in the nasal bone, sternebrae, and xiphoid cartilage.

The nasal bone of CDO null mice was typically observed to be contorted (Figure 7a). None of the male wild-type mice were seen to have the contorted nasal bone, whereas 38% of the male CDO null mice exhibited the contorted nasal bone (Figure 8). Female mice had slightly different outcomes; 17% of wild-type female mice and 36% of CDO null female mice were observed to exhibit the contorted nasal bone (Figure 8). A nominal likelihood ratio χ^2 test obtained from logistic regression (Table 1) confirmed significant increases ($p=0.013$) in the contorted nasal bone among all CDO null mice. No statistical significance was seen between the sex of the mice and the frequency of the contortion. This analysis also showed no significant interaction between sex and genotype.

Wild-type mice are more inclined to have a fusion between sternebrae 4 and 5 (Figure 7d, red arrows), whereas CDO null mice frequently had a separation between sternebrae 4 and 5 (Figure 7d, arrows). None of the male and female wild-type mice lacked fusion between sternebra 4 and sternebra 5 (Figure 8). In contrast, 87% and 43% of the male and female CDO null specimens, respectively, lacked fusion between sternebra 4 and sternebra 5 (Figure 8). Likelihood ratio χ^2 test obtained from logistical regression (Table 1) confirmed significant dependence of frequency of fusion on the genotype ($p<0.0001$) and on sex ($p=0.008$). This analysis also showed no significant interaction between sex and genotype. Two-tail Fisher's exact test on male and female sex effect on phenotype showed similar results (data not included).

The xiphoid cartilage is the cartilaginous extension below sternebra 6 (Figure 7d, orange arrow). In this study, 9% of the male and 42% of the female wild-type mice had a medially unfused xiphoid cartilage, whereas 69% (male) and 86% (female) of CDO null mice had a medially unfused xiphoid cartilage (Figure 8). Likelihood ratio χ^2 test obtained from logistical regression (Table 1) confirmed significant dependence of frequency of fusion on the genotype ($p<0.0001$) and on sex ($p=0.040$). This analysis also showed no significant interaction between sex and genotype. Two-tail Fisher's exact test on male and female sex effect on xiphoid cartilage fusion showed similar results (data not included).

A typical newborn mouse should have fully ossified skull, axial skeleton, and limb by the end of gestation, with the exception of the phalanx (12). In our skeletal staining study, the paired use of both Alizarin Red and Alcian Blue allowed for the identification of both ossified areas of bone and collagen-rich areas; the Alizarin Red dye was used to stain ossified bone red, whereas the Alcian Blue dye was used to stain collagen blue. Since a violet color designates an intermediate between blue and red, violet-colored femora of CDO null mice indicated poor ossification in null mice compared with wild-type mice (Figure 7b). The epiphyseal plate of the femur also demonstrated some of the same characteristics with differential staining (Figure 7c); the bluer staining in CDO null mice within the epiphyseal plate indicates incomplete ossification of the epiphyseal plate. No quantitative data on abnormal features of the femora were obtained. In contrast to skeletal staining outcomes, bone density evaluations through x-ray and DEXA scanning showed no conclusive evidence of bone density differences between wild-type and CDO null mice (data not shown).

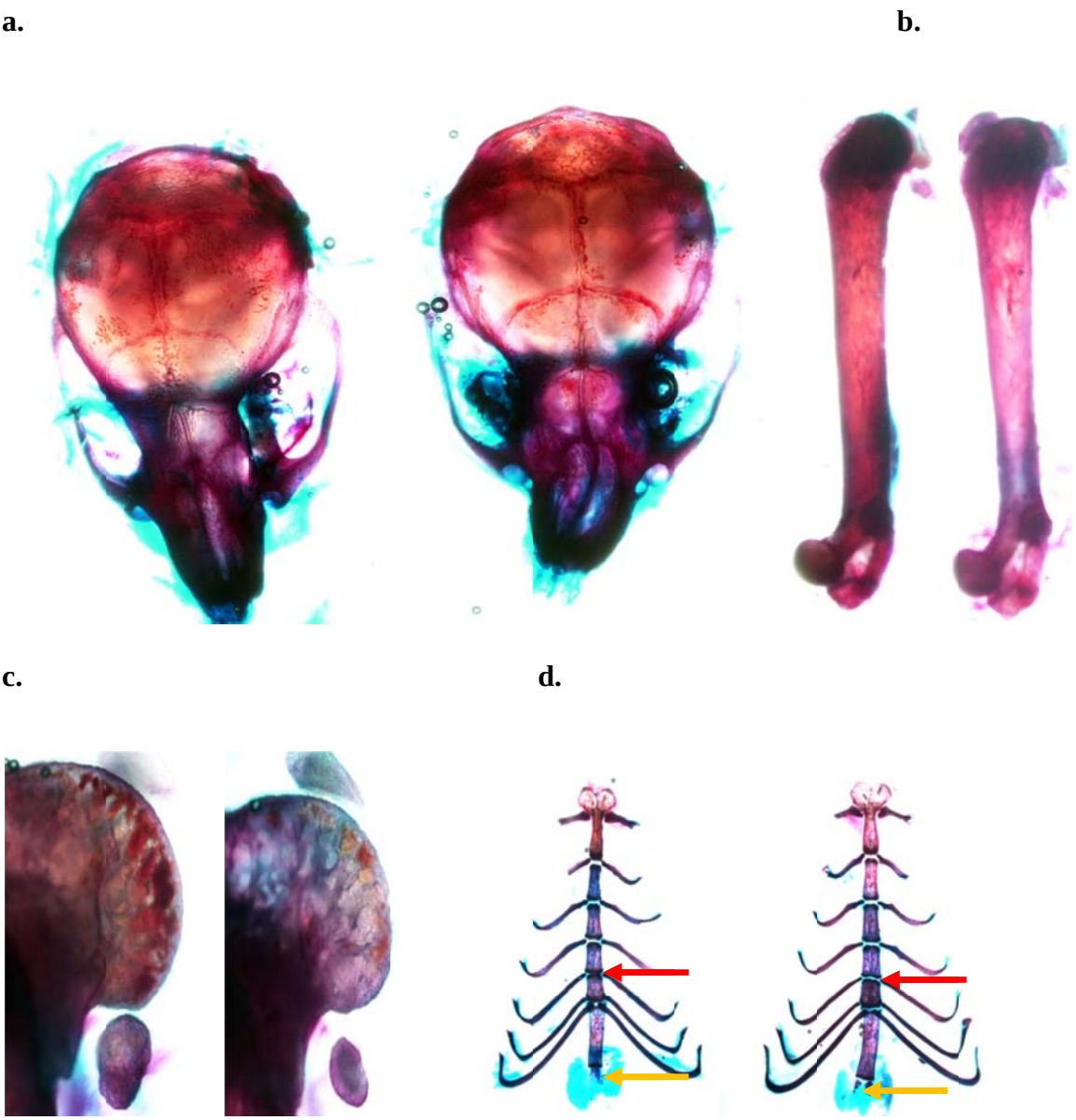

Figure 7. Stained portions of select skeletal structures. Each image pair contains a WT specimen on the left and a null specimen on the right. (a) Stained cranium; (b) Stained femur; (c) Stained epiphyseal plate; and (d) Stained sternebrae. Orange arrow points at xiphoid cartilage. Red arrows point at fusion juncture between sternebra 4 and sternebra 5.

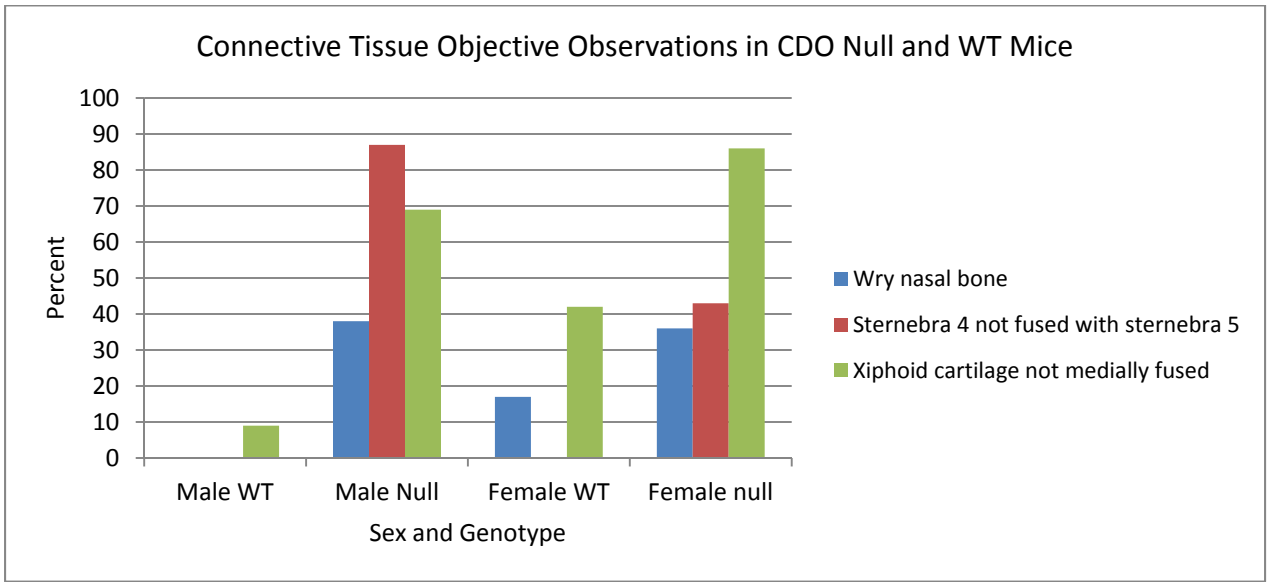

Figure 8. Graphical representation of specimens with particular traits.

	Sex	No. of Contorted (Wry) Nasal Bone	No. of Unfused Sternebra 4 with Sternebra 5	No. of Unfused Xiphoid Cartilage
WT	M	0	0	1
	F	2	0	5
	M+F	2	0	6
CDO Null	M	6	4	11
	F	5	6	12
	M+F	11	10	23
Effect		G ($p=0.013$); S (p=NS); SxG (p=NS)	G ($p<0.0001$); S ($p=0.008$); SxG (p=NS)	G ($p<0.0001$); S ($p=0.040$); SxG (p=NS)

Table 1. Number of specimens with specified traits according to sex (M=male, F=female) and genotype. Nominal likelihood ratio χ^2 test was used for statistical analysis of dependence of genotype (G), sex (S), and the interaction between sex and genotype (SxG), on phenotype outcomes. Probability of the ratio not being different from 1.0 are indicated as NS (non-significant = $p > 0.050$).

CDO null mice have significant alveolar airspace enlargement

Representative histological images of wild-type and CDO null lung stained with H&E are shown in Figure 9. Analysis of differentially stained lung sections of 8-week old CDO null mice showed enlarged alveolar airspaces. The mean linear intercept (MLI) for wild-type and/or CDO heterozygous (n=10: 4 females, 6 males) and CDO null (n=9: 4 females, 5 males) animals was measured (Figure 10) and values were compared by unpaired two-tail t-test. CDO null animals

showed a significantly larger MLI than wild-type (p=0.027). Larger MLI indicates fewer alveolar walls intercepted, thereby indicating larger alveolar airspaces and decreased surface area for gas exchange. When compared by sex, only male CDO null mice showed significantly increased airspaces compared with wild-type male mice (unpaired one-tailed t-test, p=0.031), while females CDO null mice were not significantly different from female wild-type mice (p=0.091).

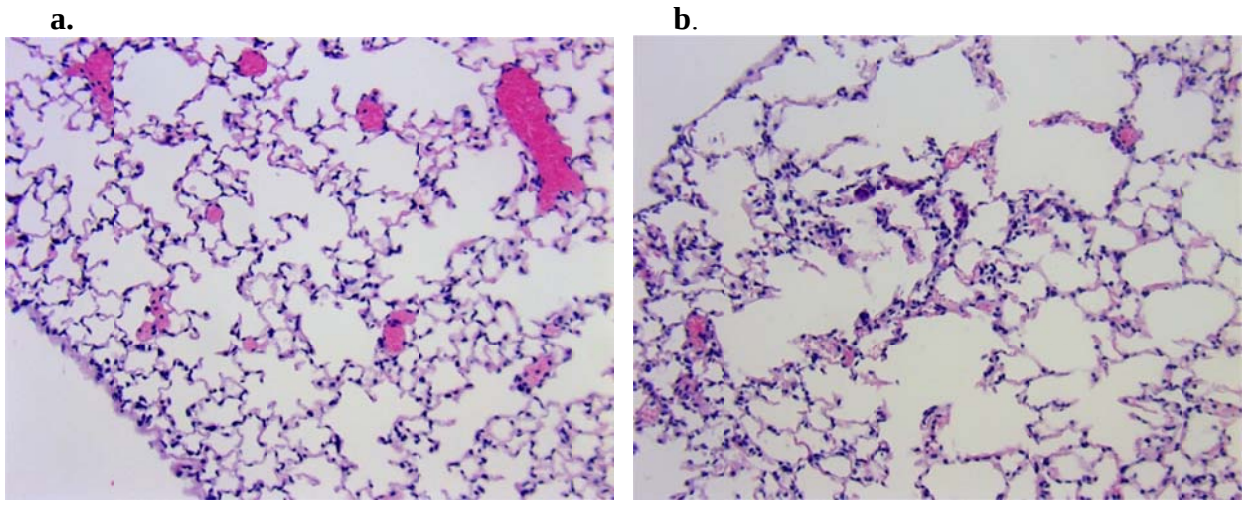

Figure 9. Lung histological staining of male WT (left image) and CDO null (right image) mice. (a) An image of lung histology in a WT mouse. (b) An image of lung histology in a CDO null mouse. Both images are at 200x magnification.

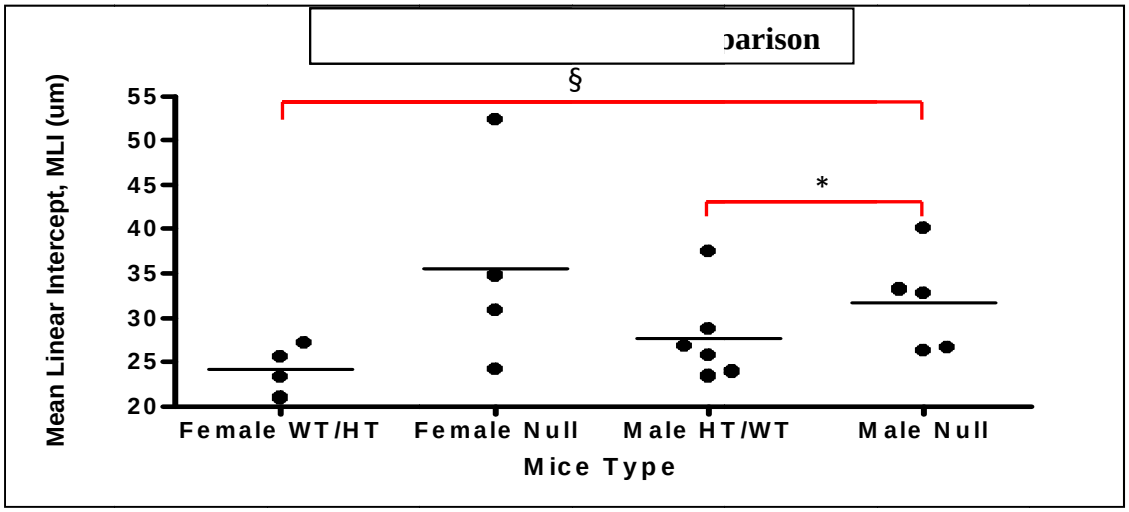

Figure 10. Composite data on mean linear intercept (μm) in 19 specimens divided by sex and by genotype. Overall, CDO null mice have significantly larger MLI (p=0.027). When compared between genders, only males had a significant increase in air space (p=0.031). Asterisk indicates $p < 0.050$. § indicates $p < 0.050$ across genotype.

Histological staining reveals elastin breakage

Using VVG staining procedures (Figure 11a-d, f), in which collagen stains red and elastic fibers (and nuclei) stain black, our histological images illustrate abnormalities in lungs of CDO null mice. Intima (posterior to the luminal endothelial cells) of both intra-acinar pulmonary vessels (Figure 11c) and larger pre-acinar pulmonary vessels (Figure 11b right) demonstrate thickened, fragmented and disorganized elastic fibers in CDO null mice. Fragmentation and tangled disarray of elastic fibers can be seen throughout the lung parenchyma in CDO null mice (Figure 11d). VVG staining revealed that the red scuff posterior to the elastic fibers is primarily composed of collagen. CDO null mice have strands of collagen that are thinner in shape compared to wild-type mice (Figure 11a and 11b). Figure 11e displays an image stained with H&E in order to show endothelial cells lining the tunica intima of blood vessels. Endothelial cells of the blood vessels are identified by the black-stained nuclei (Figure 11e, arrow). In comparison, Figure 11f is a histological image stained with VVG. VVG stains both nuclei and elastic fibers black (Figure 11f, arrow).

Further testing with Western blotting confirmed higher levels of MMP-12 (elastase; Figure 12a) in CDO null mice. Quantification demonstrated significantly higher levels of MMP-12 (one-tailed t-test; $p=0.009$; $n=6$: 3 CDO null males, 3 WT males) in male CDO null mice compared with male wild-type mice (Figure 13a). However, relative levels of MMP-9 (gelatinase) were inconclusive due to non-specific binding of MMP-9 antibodies to actin (Western blot data not included). Tissue inhibitors of matrix metalloproteinases (TIMPs) were also blotted (Figure 12b and 12c). Quantification (Figure 13b and 13c) revealed that neither TIMP-1 nor TIMP-3 protein levels were significantly greater in CDO null than in wild-type male

mice (one-tailed t-test; p=0.080 and p=0.067, respectively). On average, however, TIMP-1 protein levels tended to be higher in CDO null male mice, and TIMP-3 protein levels tended to be lower in CDO null male mice (Figure 13b and 13c). Quantitative real time RT-PCR indicated that the MMP-12 mRNA was the only mRNA (out of MMP-9, TIMP-1, and TIMP-3) to have a large mean fold-increase of 3.22 (Table 2). However, the standard deviation for the MMP-12 mRNA was about 100% of the mean fold-increase (Table 2).

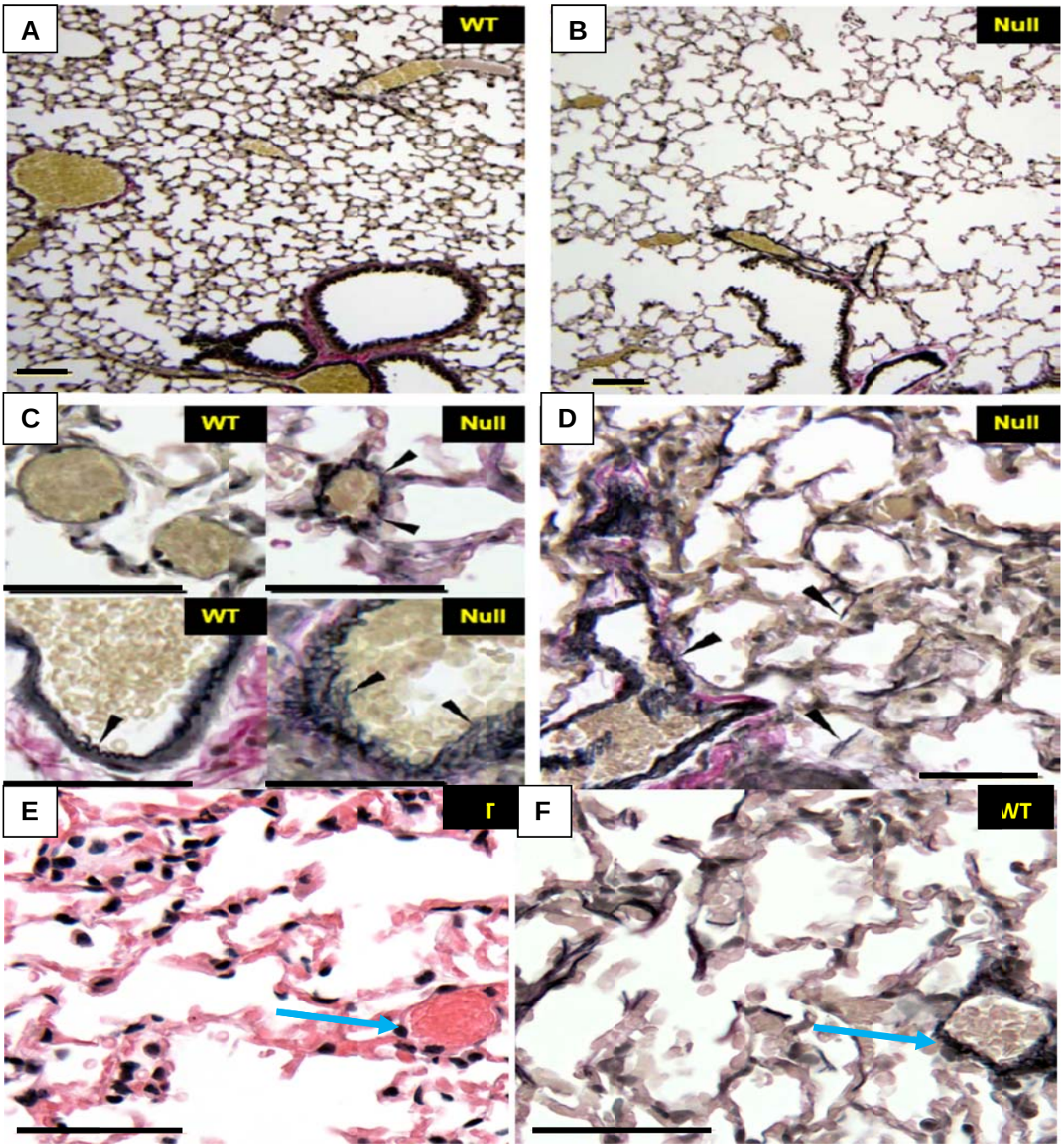

Figure 11. Histological stains of lung samples from both WT and null CDO mice. Scale bars = 50μm. (a) WT mice at 100x magnification; (b) Null mice at 100x magnification; (c) WT/Null blood vessel in lung 1000x magnification; (d) Null mice 400x magnification. Black arrowheads point to elastin; (e) H&E staining shows endothelial cells of blood vessel where blue arrow points in WT mouse lung; (f) WT mouse lung with VVG staining. Arrow points to where elastin and nuclei both stain black.

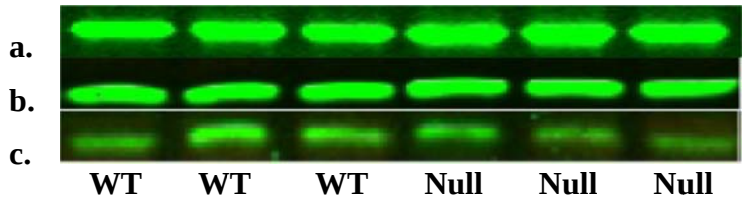

Figure 12. Western blots of MMP-12, TIMP-1, and TIMP-3 in male WT and CDO null mice. (a) MMP-12 (54 kDa); (b) TIMP-1 (23 kDa); (c) TIMP-3 (24 kDa)

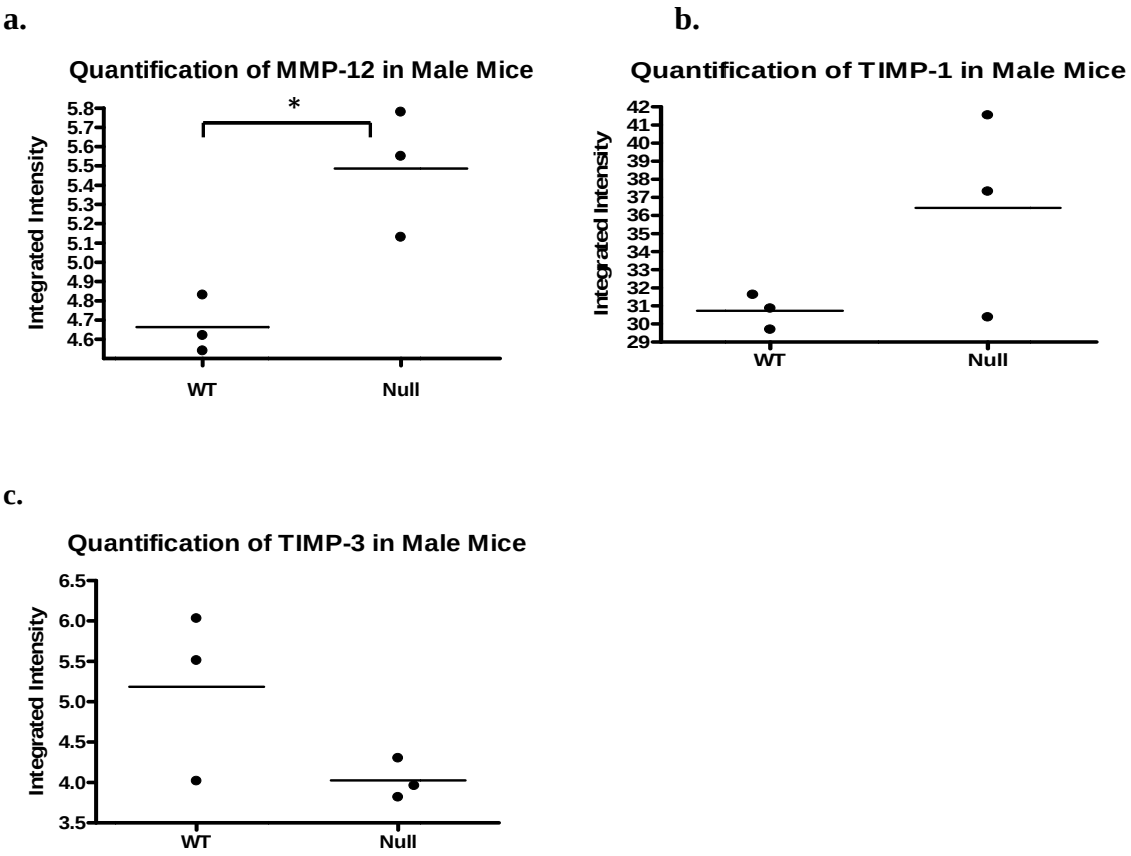

Figure 13. Quantification of (a) MMP-12; (b) TIMP-1; (c) and TIMP-3 Western blots in male CDO null and WT mice. All values are normalized for actin. Asterisk indicates $p < 0.050$.

	avg fold	stdev
MMP9	0.73	0.29
MMP12	3.22	3.33
TIMP1	0.99	0.21
TIMP3	1.35	0.07

Table 2. Quantitative real time RT-PCR quantitation of MMP-9, MMP-12, TIMP-1, and TIMP-3 mRNA. Data represents as average fold-change of mRNA along with the standard deviation. (N= 6: 3 male CDO null, 3 male WT).

Discussion

Cranial measurements indicated that NL and FL were significantly shorter in CDO null mice (except the NL of male CDO null mice) compared with wild-type mice. In contrast, NW and LR were significantly wider in CDO null mice (except the LR of female CDO null mice) compared to wild-type mice. Perhaps compensatory mechanisms are in play that widen one structure when another structure is shortened and vice-versa.

Because CDO null mice exhibited distinct nasal/cranial abnormalities and were growth-delayed (64), a close examination of skeletal structure of mice was performed. Several phenotypic differences were observed in the skeletal structure of CDO null and wild-type control mice. Bone growth delay, contorted nasal bone, bone fusion abnormalities, and abnormal ossification were observed in CDO null mice compared to wild-type mice. One abnormality was only observed in null mice and was highly predictive of null status; unfused sternebrae 4 and 5 was observed in 33% of null mice but in none of the 23 wild-type mice. In addition, the presence of a contorted nasal bone and of a medially unfused xiphoid cartilage was significantly more frequently observed in null mice. A wry nasal bone was observed in 37% of null mice but in only 9% of wild-type mice, whereas an unfused xiphoid cartilage was observed in 77% of null mice but in only 26% of wild-type mice. The delay in fusion of sternebra 4 to sternebra 5 was the most remarkable observation in the CDO null mice, but still not all CDO null mice had unfused sternebrae 4 and 5 between post natal day 51 and 64.

Interpretations of the stained femur and epiphyseal plate are limited. Differences in body mass and body composition (i.e. fat, lean, and skeletal mass) may have altered how well a

particular bone in specimens stained. These same differences may have also affected how well a particular mouse de-stained. In general, wild-type mice were "heavier" than CDO null mice, and with heavier mice, there are more skeletal muscle and adipose tissue that have to be overcome by staining and de-staining. Since all specimens were stained the same number of days, differences in staining in the femur and epiphyseal plate may be attributed to phenotypic differences (i.e. body composition) between CDO null and wild-type control mice.

Due to differences in gross appearance of skeletal structures, such as the ribs, and the preliminary observation of lower density of whole CDO null mice when analyzed by DEXA, bone mineral density determinations were made on the skeleton. DEXA scanning of the skeletons revealed no particular differences in bone mineral densities between CDO null and wild-type control mice. In addition, x-ray imaging results culminated in ambiguous results, with some CDO null mice displaying prominent hollowness in the femur and with others displaying no differences when compared to wild-type mice. One potential error in carrying out the DEXA scanning was the incomplete thawing of all mice specimens, which would have skewed density readings, as the lower densities associated with particulates of ice crystals would also lower the bone mineral density readings by the DEXA in non-thawed mice. An error that occurred with the x-ray scanning was the use of non-standardized film development. Without any calibration, our x-ray images did not differentiate between null and wild-type CDO mice. These studies would need to be repeated to make any firm conclusions.

Logically, interests in connective tissue abnormalities extended to interests into other areas where connective tissue is present. The lung was a promising outlet for our quest. Not

only is the lung readily assessable, but it is also primarily composed of connective tissues like collagen and elastin. Initial histological staining of the lungs revealed larger air space volume, as indicated by significant increases in MLI, and abnormal elastin structure throughout the lung of CDO null mice.

Our initial hypothesis that matrix metalloproteinase enzymes may be associated with these observations was confirmed by the observations that elastase (MMP-12) was selectively up-regulated in lung of CDO null mice. In contrast, expression of gelatinase (MMP-9), TIMP-1, and TIMP-3 were not significantly affected by genotype. Western blotting confirmed that MMP-12 protein was significantly increased in null mice, as was the trend for MMP-12 mRNA. An obvious limitation in the immunoblotting study was the use of only male specimens. In addition, although immunoblotting allowed quantification of the abundance of MMPs and TIMPs, definitive confirmation of localized increases in MMPs using immunohistochemical procedures would be valuable in future studies.

The relations of these phenotypic differences in CDO null mice are presumably related in some way to the metabolic phenotype generated by loss of CDO, a key enzyme in the oxidative metabolism of cysteine to its end products, taurine and sulfate. CDO null mice have been characterized to have extremely low plasma and tissue taurine levels, along with slightly elevated plasma and tissue cysteine levels, supporting the predictive effects of lacking cysteine flux through the CDO metabolic pathway (64). Taurine supplementation in CDO null mice improved survival of male pups with no effect on the phenotype of CDO null mice. Speculations of cysteine catabolism through an alternative pathway, namely the desulfhydration pathway, arose

when plasma sulfate (downstream product of cysteine catabolism) and sulfide were found to be slightly elevated in CDO null mice compared with wild-type mice. Sulfide is a product of cysteine catabolism through the cystathionine β-synthase and cystathionine γ-lyase desulfhydration pathways. Hydrogen sulfide (H_2S) has dual roles as a signaling molecule and as a toxicant. Thus, pathology seen in connective tissue of CDO null mice may be associated with dysregulation of H_2S. Yet studies have implicated beneficial effects of H_2S. H_2S use has been suggested as a therapeutic agent for lung injury (50). Whether or not H_2S affects skeletal structures is not known.

CDO null mice also have decreased levels of hepatic cytochrome c oxidase, an enzyme involved in the electron transport chain (64). Compounding lower levels of hepatic cytochrome c oxidase in CDO null mice is the inhibitory effects of H_2S on cytochrome c oxidase (51). Altogether, this suggests a possible effect of the alteration in the electron transport system of CDO null mice on its phenotype.

A hypothesized link between loss-of-function mutations in CDO and the incidence of rheumatoid arthritis has existed for several decades and was largely based on observed increases in the cysteine-to-sulfate ratio in the plasma and low levels of sulfate in synovial fluid of patients with this disease (52). High plasma cysteine-to-plasma inorganic sulfate ratios were presumed to alter sulfate conjugation reactions, providing a clear link to the highly sulfated proteoglycans in the extracellular matrix or connective tissues (52,55,56). The observations on the CDO null mouse, however, suggest that loss-of-function mutations of CDO do not cause a depletion of sulfate, at least in mice. Cysteine-to-sulfate ratios in CDO null mice did increase slightly, due to

the greater accumulation of cysteine than of sulfate, whereas the cysteine to taurine ratios were dramatically higher in null mice and would seem to be a much better indicator of lack of CDO activity. In addition, damage observed in CDO null mice could be associated with the increased production of H_2S and other reduced sulfur compounds (e.g., persulfides) due to the block in the conversion of cysteine to cysteinesulfinate and cysteinesulfinate's further metabolism to hypotaurine/taurine and sulfite/sulfate.

Other studies have found that cysteine drives the synthesis of pro-inflammatory leukotriene-cysteinyl adducts, which have a function in the proliferation and contraction of smooth muscle cells in the lung, migration of eosinophils, and damage to the mucus layer of the lung (57,58,59). Recruitment of eosinophils to the lung, along with their activation, releases effector inflammatory cytokines and growth factors like interleukin-1 (IL-1), tumor necrosis factor- α (TNF-α), transforming growth factor- β (TGF-β), and vascular endothelial growth factor (VEGF). These effector molecules have been demonstrated to up-regulate the transcription of MMP-12 (60,61). Since the predictive effect of up-regulating the transcription of MMP-12 is the increase in elastin breakdown, the up-regulation of MMP-12 transcription may explain the pathology seen in our CDO null mice. During inflammatory responses, H_2S has been suggested to play a role in recruiting neutrophils (62). Increases in MMP-12 in our lung specimens may be a result of increased neutrophil accumulation in CDO null mice since neutrophils secrete MMP-12 upon activation. Moreover, the pathology of the lungs of CDO null mice may exacerbate conditions through resistive breathing patterns in the mice.

Inspiratory resistive breathing patterns up-regulate cytokine production of interleukin-6 (IL-6), TNF-α, and interleukin-2 (IL-2) in the diaphragm (63). Abnormal lung histology of the CDO null mice suggests an impaired ability to breathe in these same mice, which may perpetuate the pathology of CDO null mice lung; inflammatory cytokines induced upon resistive breathing up-regulate the expression of MMP-12, which may result in the disarray seen in CDO null mice lung histology. Further work may be conducted to understand the connection between resistive breathing pattern and the pathology of the CDO null mouse.

To better understand the connection between CDO null mice and connective tissue pathology, work on establishing the function of impairments in the CDO catabolic pathway on skeletal development should also be conducted. Furthermore, investigating how abnormal taurine, cysteine, and sulfide levels in CDO null mice are associated with the inflammatory up-regulation of MMPs would highlight key cytokines responsible for MMP up-regulation in CDO null mice. This study only investigated two select MMP proteins out of the 25 or more MMPs that are known to exist. Similarly, only two of the four TIMPs were studied. Other venues of interest should be directed towards the investigation of which MMPs and TIMPS have prominent associations with CDO null mice morphology and pathology.

References

1. Stipanuk, MH. Biochemical and Physiological Aspects of Human Nutrition. Philadelphia: W.B. Saunders Co., 2000. pp. 395-398.
2. Bella DL, Stipanuk MH (1995) Effects of protein, methionine, or chloride on acid-base balance and on cysteine catabolism. *Am J Physiol* 269: E910–E917.
3. Bella DL, Hahn C, Stipanuk MH (1999) Effects of nonsulfur and sulfur amino acids on the regulation of hepatic enzymes of cysteine metabolism. *Am J Physiol* 277: E144-153.
4. Lee JI, Londono M, Hirschberger LL, Stipanuk MH (2004) Regulation of cysteine dioxygenase and gamma-glutamylcysteine synthetase is associated with hepatic cysteine level. *J Nutr Biochem* 15: 112-122.
5. Stipanuk MH, Londono M, Lee JI, Hu M, Yu AF (2002) Enzymes and metabolites of cysteine metabolism in nonhepatic tissues of rats show little response to changes in dietary protein or sulfur amino acid levels. *J Nutr* 132: 3369-3378.
6. Davies MH, Ngong JM, Pean A, Vickers CR, Waring RH, Elias E (1995) Sulphoxidation and sulphation capacity in patients with primary biliary cirrhosis. *J Hepatol* 22: 551–60.
7. Waring RH, Ramsden DB, Wilkinson LJ, and Kikuchi H (2007) Polymorphism in Cysteine Dioxygenase. International Publication Number WP 2007/010258 A2. World Intellectual Property Organization.
8. Olsen BR, Reginato AM, Wang W (2000) Bone development. *Annu Rev Cell Dev Biol* 16: 191–220.
9. Langille RM (1994) Chondrogenic differentiation in cultures of embryonic rat mesenchyme. *Microsc Res Tech* 28: 455-469.
10. Chen JM (1952) Studies on the morphogenesis of the mouse sternum. I. Normal embryonic development. *J Anat* 86: 373-386.
11. Otis EM, Brent R (1954) Equivalent ages in mouse and human embryos. *Anat Rec* 120: 33-53.
12. Fritz H, Hess R (1970) Ossification of the rat and mouse skeleton in the perinatal period. *Teratology* 3: 331-338.
13. Cormack, David H. Ham's Histology, 9th ed. Philadelphia: J.B. Lippincott Company. 1987. pp. 551-562.
14. Di Fiore, Mariano S.H, Eroschenko, Victor, Ed. Atlas of Normal Histology, 6th ed. Philadelphia: Lea & Febiger. 1988. p. 86.
15. Chin JR, Werb Z (1997) Matrix metalloproteinases regulate morphogenesis, migration and remodeling of epithelium, tongue skeletal muscle and cartilage in the mandibular arch. *Development* 124:1519–30.
16. Johansson N, Saarialho-Kere U, Airola K, Herva R, Nissinen L, Westermarck J, Vuorio E, Heino J, Kähäri V-M (1997) Collagenase-3 (MMP-13) is expressed by hypertrophic chondrocytes, periosteal cells, and osteoblasts during human fetal bone development. *Dev Dyn* 208: 387-397.
17. Shapiro SD (1998) Matrix metalloproteinase degradation of extracellular matrix: biological consequences. *Curr Opin Cell Biol* 10: 602-608.
18. Abdallah MA, Nakajima ST, Lin PC, Gercel-Taylor C (2005) Plasma matrix metalloproteinase activity during the menstrual cycle of healthy ovulatory patients who underwent tubal ligation. *Fertil Steril* 84: 1766–1767.
19. Rundhaug JE (2003) The biology behind matrix metalloproteinases, angiogenesis and cancer. *Clin Cancer Res* 9: 551-554.
20. Lorente L, Martin MM, Sole-Violan J, Blanquer J, Paramo JA (2010) Matrix metalloproteinases and their inhibitors as biomarkers of severity in sepsis. *Crit Care* 14: 402.
21. Vincenti MP, Brinckerhoff CE (2002) Transcriptional regulation of collagenase (MMP-1, MMP-13) genes in arthritis: integration of complex signaling pathways for the recruitment of gene-specific transcription factors. *Arthritis Res* 4: 157–164.
22. Egeblad M, Werb Z (2002) New functions for the matrix metalloproteinases in cancer progression. *Nature Rev Cancer* 2: 161-174.
23. Van Lint P, Libert C (2007) Chemokine and cytokine processing by matrix metalloproteinases and its effect on leukocyte migration and inflammation. *J Leukoc Biol* 82 (6): 1375–81.
24. Nyormoi O, Mills L, Bar-Eli M (2003) An MMP-2/MMP-9 inhibitor, 5a, enhances apoptosis induced by ligands of the TNF receptor superfamily in cancer cells. *Cell Death Differ* 10: 558–569.
25. Pei D (2005) Matrix metalloproteinases target protease-activated receptors on the tumor cell surface. *Cancer Cell* 7: 207–208.
26. Everts V, Delaisse JM, Korper W, Beertsen W (1998) Cysteine proteinases and matrix metalloproteinases play distinct roles in the subosteoclastic resorption zone. *J Bone Miner Res* 13:1420–30.

27. Holliday LS, Welgus HG, Fliszar CJ, Veith GM, Jeffrey JJ, Gluck SL (1997) Initiation of osteoclast bone resorption by interstitial collagenase. *J Biol Chem* 272:22053–8.
28. Sternlicht M D, Werb Z (2001) How matrix metalloproteinases regulate cell behavior. Annu. Rev. Cell Dev. Biol. 17, 463–516.
29. Snoek-van Beurden PA, Von den Hoff JW (2005) Zymographic techniques for the analysis of matrix metalloproteinases and their inhibitors. *Biotechniques* 38:73– 83.
30. Vu TH, Z Werb (1998) Gelatinase B: structure, regulation, and function. In: Biology of Extracellular Matrix-Matrix Metalloproteinases. William C. Parks and Robert P. Mecham, eds., San Diego: Academic Press. 1998. pp. 115-148.
31. Tschesche H, Knäuper V, Kramer S, Michaelis J, Oberhoff R, Reinke H (1992) Latent collagenase and gelatinase from human neutrophils and their activation. *Matrix Suppl* 1: 245–255.
32. Ståhle-Bäckdahl M, Parks W C (1993) 92-kDa gelatinase is actively expressed by eosinophils and stored by neutrophils in squamous cell carcinoma. *Am J Pathol* 142: 995–1000.
33. Vaalamo M, Kariniemi AL, Shapiro SD, Saarialho-Kere U (1999) Enhanced expression of human metalloelastase (MMP-12) in cutaneous granulomas and macrophage migration *J Invest Dermatol* 112: 499–505.
34. Nénan S, Boichot E, Lagente V, Bertrand CP (2005) Macrophage elastase (MMP-12): a pro-inflammatory mediator? *Mem Inst Oswaldo Cruz* 100(Suppl 1): 167 – 172.
35. Wert SE, Yoshida M, LeVine AM, Ikegami M, Jones T, Ross GF, Fisher JH, Korfhagen TR, Whitsett JA (2000) Increased metalloproteinase activity, oxidant production, and emphysema in surfactant protein D gene-inactivated mice. *Proc Natl Acad Sci USA* 97:5972–5977.
36. Tetley TD (2002) Macrophages and the pathogenesis of COPD. *Chest* 121: 156S-159S.
37. Brew K, Dinakarpandian D, Nagase H (2000) Tissue inhibitors of metalloproteinases: evolution, structure and function. *Biochim Biophys Acta* 1477:267–283.
38. Visse R, Nagase H (2003) Matrix metalloproteinases and tissue inhibitors of metalloproteinases: structure, function, and biochemistry. *Circ Res* 92:827–839.
39. Gasson JC, Golde DW, Kaufman SE, Westbrook CA, Hewick RM, Kaufman RJ, Wong GG, Temple PA, Leary AC, Brown EL (1985) Molecular characterization and expression of the gene encoding human erythroid-potentiating activity. *Nature* 315: 768–771.
40. Stetler-Stevenson WG, Bersch N, Golde DW (1992) Tissue inhibitor of metalloproteinase-2 (TIMP-2) has erythroid-potentiating activity. *FEBS Lett* 296: 231–234.
41. Black RA (2004) TIMP3 checks inflammation. *Nature Genet* 36: 934–935.
42. Vacek TP, Gillespie W, Tyaqi N, Vacek JC, Tyaqi SC (2010) Hydrogen sulfide protects against vascular remodeling from endothelial damage. *Amino Acids* 39 (5): 1161-9.
43. Knäuper V, Will H, Lopez-Otin C, Smith B, Atkinson SJ, Stanton H, Hembry RM, Murphy G (1996) Cellular mechanisms for human procollagenase-3 (MMP-13) activation. Evidence that MT1-MMP (MMP-14) and gelatinase a (MMP-2) are able to generate active enzyme. *J Biol Chem* 271: 17124–17131.
44. Apte SS, Olsen BR, Murphy G (1995) The gene structure of tissue inhibitor of metalloproteinases (TIMP)-3 and its inhibitory activities define the distinct TIMP gene family. *JBiol Chem* 270: 14313–14318.
45. Depew MJ (2008) Analysis of skeletal ontogenesis through differential staining of bone and cartilage. *Methods Mol Biol* 461: 37-45.
46. Kawakami M, Yamamura K-I (2008) Cranial bone morphometric study among mouse strains. *BMC Evolutionary Biology* 8: 73.
47. Dunnill MS (1962) Quantitative Methods in the Study of Pulmonary Pathology. *Thorax* 17: 320-328.
48. Hamelet J, Maurin N, Fulchiron R, Delabar JM, Jane N (2007) Mice lacking cystathionine beta synthase have lung fibrosis and air space enlargement. *Experimental and Molecular Pathology* 83: 249-253.
49. Pfaffl MW (2001) A new mathematical model for relative quantification in real-time RT-PCR. *Nucleic Acids Res* 20: 2002-2007.
50. Esechie A, Kiss L, Olah G, Horvath EM, Hawkins H, Szabó C, Traber DL (2008) Protective effect of hydrogen sulfide in a murine model of acute lung injury induced by combined burn and smoke inhalation. *Clin Sci (Lond)* 115: 91-97.
51. Dorman DC, Moulin FJ-M, McManus BE, Mahle KC, James RA, Struve MF (2002) Cytochrome oxidase inhibition induced by acute hydrogen sulfide inhalation: correlation with tissue sulfide concentrations in the rat brain, liver, lung, and nasal epithelium. *Toxicol. Sci* 65: 18–25.

52. Bradley H, Gough A, Sokhi RS, Hassell A, Waring R, Emery P (1994) Sulfate metabolism is abnormal in patients with rheumatoid arthritis: confirmation by in vivo biochemical findings. *J. Rheumatol* 21:1192-96.
53. Miklos S (1995) Dehydroepiandrosterone sulfate in the diagnosis of osteoporosis. *Acta BioMedica de L'ateneo Parmense* 66: 139–146.
54. Parker LN (1991) Control of adrenal androgen secretion. *Endocrinol Metab Clin North Am* 20: 401-421.
55. Heafield MT, Fearn S, Steventon GB, Waring RH, Williams AC, Sturman SG (1990) Plasma cysteineand sulphate levels in patients with motor neurone, Parkinson's and Alzheimer's disease. *Neurosci Lett* 110: 216–20.
56. Scadding GK, Ayesh R, Brostoff J, Mitchell SC, Waring RH, Smith RL (1988) Poor sulphoxidation ability in patients with food sensitivity *Br Med J* 297: 105–7.
57. Csoma Z, Kharitonov SA, Balint B, Bush A, Wilson NM, Barnes PJ (2002) Increased leukotrienes in exhaled breath condensate in childhood asthma. *Am J Respir Crit Care Med* 166(10): 1345–9.
58. Obshima N, Nagase H, Koshino T et al (2002) A functional study on CysLT(1) receptors in human eosinophils. *Int Arch Allergy Immunol* 129(1): 67–75.
59. Arango P, Borish L, Frierson HF Jr, Kountakis SE (2002) Cysteinyl leukotrienes in chronic hyperplastic rhinosinusitis. *Otolaryngol Head Neck Surg* 127(6): 512–15.
60. Kerkela E, Bohling T, Herva R, Uria JA, Saarialho-Kere U (2001) Human macrophage metalloelastase (MMP-12) expression is induced in chondrocytes during fetal development and malignant transformation. *Bone* 29: 487–93.
61. Feinberg MW, Jain MK, Werner F, *et al* (2000) Transforming growth factor-beta 1 inhibits cytokine-mediated induction of human metalloelastase in macrophages. *J Biol Chem* 275: 25 766–25 773.
62. Dal-Secco D, Cunha TM, Freitas A, Alves-Filho JC, Souto FO, Fukada SY, Grespan R, Alencar NM, Neto AF, Rossi MA, Ferreira SH, Hothersall JS, Cunha FQ (2008) Hydrogen sulfide augments neutrophil migration through enhancement of adhesion molecule expression and prevention of CXCR2 internalization: role of ATP-sensitive potassium channels. *J Immunol* 181**:** 4287-4298.
63. Vassilakopoulos T, Katsaounou P, Karatza MH, Kollintza A, Zakynthinos S, Roussos C (2002) Strenuous resistive breathing induces plasma cytokines: role of antioxidants and monocytes. *Am J Respir Crit Care Med* 166:1572–1578.
64. Ueki I, Roman HB, Valli A, Fieselmann K, Lam J, Peters R, Hirschberger LL, and Stipanuk MH. Knockout of the murine cysteine dioxygenase gene results in severe impairment in ability to synthesize taurine and an increased catabolism of cysteine to hydrogen sulfide. *Am J Physiol Endocrinol Metab*, in press.